Effect of Bi$_{0.2}$Sr$_{0.7}$SnO$_3$ doping on NaNbO$_3$-based ceramics: enhanced ferroelectric, dielectric, and energy storage performance

Yuqing Chen[1] , XinRong Zhong[1], Anze Shui[1,*], and Chao He[1,*]

[1] *School of Materials Science and Engineering, South China University of Technology, Guangzhou 510641, PR China*

ABSTRACT

NaNbO$_3$-based antiferroelectric ceramics are considered to be popular candidates for lead-free dielectric capacitors. However, the instability of the antiferroelectric phase of pure NaNbO$_3$ (NN) ceramics under high electric fields leads to poor energy storage density and efficiency. Therefore, in order to stabilize the antiferroelectric phase of NN, $(1 - x)$NaNbO$_3$-xBi$_{0.2}$Sr$_{0.7}$SnO$_3$ [$(1 - x)$NN-xBSS] ($x = 0.06$–0.20) system was successfully prepared by the solid-state reaction method. The solid solution transforms from the antiferroelectric phase (AFE) to the paraelectric phase (PE) with increasing BSS doping. In addition, the Curie temperature (T_m) changes abruptly from nearly 250 °C to -120 °C at $x = 0.10$ and exhibits relaxation behavior. The best performance with a recoverable energy density (W_{rec}) of 0.80 J/cm^3 and efficiency (η) of 80.2% in this system is obtained simultaneously at 180 kV/cm in the component with $x = 0.10$. Furthermore, the 0.90NN-0.10BSS ceramic has good frequency stability. This work provides a new doping strategy and systematically investigates phase structure, microscopic morphology, and macroscopic electrical properties of $(1 - x)$NN-xBSS ceramics.

1 Introduction

In power electronic systems like pulsed power weapons, electric vehicles, and aircraft, dielectric energy storage capacitors play an important role [1, 2]. Nevertheless, dielectric capacitors have poor energy storage density, which significantly limits their commercial application. Additionally, another aspect to take into account is the environment-friendly characteristic. Therefore, in order to meet the growing demand for dielectric capacitors, it is imperative to investigate novel high-performance and environment-friendly dielectric materials [3].

By integrating the polarization–electric field (P–E) loops, the total energy storage density (W), recoverable energy density (W_{rec}), and energy storage efficiency (η) of dielectric materials can be calculated (1–3) [4–6]:

Address correspondence to E-mail: shuianze@scut.edu.cn; hechao929@scut.edu.cn

$$W = \int_0^{P_{max}} E dP, \tag{1}$$

$$W_{rec} = \int_{P_r}^{P_{max}} E dP, \tag{2}$$

$$\eta = \frac{W_{rec}}{W} \times 100\%, \tag{3}$$

where E is the external electric field, P_{max} and P_r represent maximum polarization and remnant polarization, respectively. Therefore, high dielectric breakdown strength (E_b), high P_{max}, and low P_r are generally expected to achieve high recoverable energy density and efficiency.

Traditional linear dielectric materials have extremely high efficiency, but their small permittivity restricts the growth of energy storage density [7]. Nonlinear dielectric materials, such as ferroelectrics (FE), antiferroelectrics (AFE), and relaxor ferroelectrics (RFE), are promising for energy storage applications [8–10]. Among them, AFEs are considered to be the leading candidates for energy storage capacitors due to their high P_{max} and low P_r. AgNbO$_3$-based (AN) and NaNbO$_3$-based (NN) ceramics are the most common lead-free AFE systems [11–13]. The AN ceramics present typical double hysteresis loops, which are associated with large polarization in a high electric field. In general, pure AN reached a relatively high W_{rec} of 1.6–2.1 J/cm^3 and η around 40% [14–16], but its expensive raw materials and special sintering atmosphere hindered widespread usage.

NaNbO$_3$ ceramics have the advantages of low cost, lightweight, and non-toxicity. NN ceramics undergo a series of phase transitions as the temperature decreases: Cubic (U, Pm-3m), Tetragonal (T$_2$, P4/mbm), Orthorhombic (T$_1$, Ccmm), Orthorhombic (S, Pnmm), Orthorhombic (R, Pnma), Orthorhombic (P, Pbma), and Rhombohedral (N, R3c) [17, 18], where U, T$_2$, T$_1$, and S are paraelectric (PE) phases, P and R are the AFE phases, and N is the FE phase [19, 20]. When a large external electric field is applied to pure NaNbO$_3$, the AFE P phase tends to irreversibly transform into the FE Q phase, resulting in

ferroelectric-like square hysteresis loops [21]. Therefore, pure NN materials have poor energy storage density and efficiency (W_{rec}=0.4 J/cm^3, η = 10%) [22].

In order to solve this problem, researchers have made a lot of ideas about how to stabilize the antiferroelectric phase. In summary, it was found that the following two main factors affect the stability of the ferroelectric and antiferroelectric phase: One is to reduce the tolerance factor (t) that is calculated by following Eq. (4) [23]:

$$t = \frac{(R_A + R_o)}{\sqrt{2}(R_B + R_o)}, \tag{4}$$

where R_A, R_B, and R_O are the average ionic radii of the A-site cation, B-site cation, and oxygen anion, respectively. For AFEs, the tolerance factor is usually less than 1 and lowering the tolerance factor is more favorable to the creation of antibody distortion. For instance, the addition of SrZrO$_3$ and CaZrO$_3$ to NN-based ceramics reduced the tolerance factor, enhancing the stability of the antiferroelectric phase [17, 24, 25]. Pan et al. reduced the tolerance factor by introducing BiFeO$_3$-BaTiO$_3$ into NN-based ceramics, achieving a high energy storage density of 14.5 J/cm^3 and an energy storage efficiency of 83.9% [26]. Another important strategy for stabilizing the antiferroelectric phase is to reduce the polarization rate of the B-site ions. A low ion polarization rate helps to enhance ionic bonding, especially by producing short-range ordered polar clusters, reducing P_r, and improving energy storage efficiency [27]. Therefore, the strategy of reducing the tolerance factor or reducing the polarization of B-site ions through component modification to stabilize the antiferroelectric P phase and therefore increase energy storage density is an important research area for NN-based ceramics in the future. In addition, in order to solve the problem of low energy storage efficiency caused by the large polarization hysteresis and residual polarization of NN-based ceramics, researchers have developed the NN-BiMeO$_3$ ceramic system by referring to the experience of BiScO$_3$-PbTiO$_3$ system in the field of piezoelectricity. The NN-BiMeO$_3$ ceramic system has weakly coupled relaxation characteristics and nearly linear polarization response under electric fields, so its energy storage efficiency can be significantly improved. For example, introducing

$(Bi_{0.5}La_{0.5})(Mg_{2/3}Ta_{1/3})O_3$ into NN, resulting in strong relaxation properties [28]. Pan et al. constructed a relaxation strategy by introducing $Bi(Ni_{2/3}Nb_{1/6}Ta_{1/6})O_3$, which significantly improved the energy storage characteristics of NN-based ceramics (W_{rec}=3.43 J/cm^3, η = 83.3%) [29].

Based on the above studies, $Bi_{0.2}Sr_{0.7}SnO_3$ was introduced into pure $NaNbO_3$ (($1-x$)$NaNbO_3$—$xBi_{0.2}Sr_{0.7}SnO_3$ prepared by solid-state reaction, x = 0.06–0.20, abbreviated as $(1-x)$NN-xBSS). Firstly, as the doping amount of BSS increases, the tolerance factor decreases from 0.9633 to 0.9545, which is beneficial for stabilizing the antiferroelectric phase. In addition, the hybridization of the $6s^2$ orbital of Bi and the 2p orbital of O tends to form solitary electron pairs, which leads to the distortion of the structure, and then improves the polarization of the A-site. Secondly, the introduced B-site ion (Sn^{4+}) has a lower polarizability, which is beneficial for enhancing ion bonds and reducing the residual polarization intensity P_r. The relevant ion radius and polarization rates are shown in Table 1. Finally, the addition of cations (Bi^{3+}, Sr^{2+}, Sn^{4+}) that are not equivalent to Na^+ and Nb^{5+} leads to local charge imbalances and structural distortions that disrupt the long-range ordering of $NaNbO_3$ ceramics, transforming large-scale domains into polar nano-regions (PNRs) in favor of improved energy storage properties.

2 Experimental section

2.1 Sample Preparation

The traditional solid-state reaction technique was applied to prepare the $(1-x)$ NN- xBSS (x = 0.06, 0.10, 0.15, 0.20). These raw materials (Na_2CO_3 (99.99%), Nb_2O_5 (99.99%), SrO (99.99%), Bi_2O_3 (99.99%), and SnO_2 (99.5%) were mixed and ball milled for 10 h with using ethanol. After drying, the mixtures were calcined at 1000 °C in the air for 3 h.

Table 1 The ionic radius and polarizability of some A-site and B-site ions [30]

Ions	Na$^+$	Sr^{2+}	Bi^{3+}	Nb^{5+}	Sn^{4+}
Polarizability (Å^3)	0.309	1.3	3.949	3.1	1.798
Radius (Å)	1.39	1.44	1.31	0.64	0.69

The calcined powders were milled again and pressed (130 MPa) into disks with a 15 mm diameter using polyvinyl alcohol (PVA) as a binder. After burning off PVA, the disks were sintered at 1300–1370 °C for 2 h. In the meantime, these samples were buried in the corresponding calcined powders during the sintering procedure, and the double-crucible method was used to decrease the evaporation of elemental Na and Bi. Then, the sintered samples were polished to a thickness of ∼ 0.2 mm, they were coated with a silver paste to characterize their electric properties.

2.2 Material characterization

The crystal structures of the samples were characterized by X-ray diffraction (XRD, X'Pert, Holland) using Cu-Kα radiation. Crystal structure and lattice parameters of ceramics were analyzed using Rietveld refinement with GSAS software. The Raman spectrums were achieved using a Raman spectrometer (Renishaw Ramoscope, Invia) with an excitation source of 532 nm. The microstructure of the sintered ceramics was characterized using a field emission scanning electron microscope (FESEM, the Netherlands NOVA NANOSEM 430). The temperature dependence of permittivity (ε_r) and dielectric loss (tanδ) from − 150 °C to 300 °C were tested by a variable temperature dielectric tester (GWJDN-1000, Jingke, Beijing, China) with a frequency range of 100 Hz to 1 MHz. Using an impedance analyzer (Agilent 4294 A, Agilent, USA) / equipped with a cryostat to measure impedance spectrum over frequencies from 1 kHz to 10 MHz. The polarization–electric field (P–E) hysteresis loops were measured at 10 Hz using a commercial ferroelectric analyzer (TF Analyzer 3000, aixACCT, Aachen, Germany). The energy release properties of ceramic capacitors were investigated via a commercial charge–discharge platform (CFD-003, Tongguo, Shanghai, China) with a certain discharge resistance, inductance, and capacitance (RLC) load circuit.

3 Results and discussion

3.1 Phase and microstructure

The crystal structure of $(1-x)$ NN-xBSS ceramics are investigated using XRD analysis, as shown in Fig. 1a. All the samples display a pure perovskite structure

and no other secondary phase, proving that the $Bi_{0.2}Sr_{0.7}SnO_3$ can well diffuse into the $NaNbO_3$ lattice. To further study the phase structure of the system, the magnified spectrum near 32.5° and 46.5° is demonstrated. The average radius of $(Bi_{0.2}Sr_{0.7})^{2+}$ (1.28 Å) is smaller than Na^+ (1.39 Å) at the A-site and Sn^{4+} (0.69 Å) is larger than Nb^{5+} (0.64 Å) at B-site. However, the peaks of (110) and (200) move toward low angles with the doping of BSS, which is due to the lattice volume expansion according to the Bragg diffraction equation. Thus, the effect of cationic radius at the B-site on lattice volume is larger than that at the A-site. The splitting (110) and (200) diffraction peaks are observed in the 0.94NN−0.06BSS near 32.5° and 46.5°. As the BSS content increases, the split diffraction peaks merge into a single peak, respectively, indicating the phase transition from the orthorhombic phase to the pseudo-cubic phase. Other NN-based systems reported similar phenomena [31]. Rietveld refinement is applied to XRD patterns via GSAS software [32] with orthorhombic AFE phase (Pbma) and tetragonal PE phase (P4/mbm). The Rietveld refinement plots are shown in Fig. 2a–d. The low-reliability factors (R_{wp}<10%, $x^2 < 2.25$) indicate that the selected models are completely accepted. Figure 1b shows the bulk density, theoretical density, and relative density of $(1 − x)$NN-xBSS ceramics. The bulk density can be measured by the Archimedes method. The bulk density of $(1 − x)$NN-xBSS ceramics tend to increase with the increase of BSS doping, which is due to the fact that the relative molecular mass of $Bi_{0.2}Sr_{0.7}SnO_3$

is larger than that of $NaNbO_3$. When BSS dissolves into the NN lattice, it will make a certain contribution to the increase in mass. In addition, based on their relative density being higher than 95%, proves that all samples have high densification after high-temperature sintering.

Using the Raman spectra, the phase structure of $(1 − x)$NN-xBSS ceramics is further confirmed (Fig. 3). When x is 0.06 and 0.10, multiple peak features ($v4$, $v5$, $v6$, $v7$) are observed in 100–300 cm^{-1}, which are AFE P phase characteristics associated with oxygen octahedral tilts and Nb–O bond vibrations [33]. When $x \geq 0.15$, the peak ($v4$, $v5$, $v6$, $v7$) merge into a single peak due to the AFE P phase decreases. In the range of 300 $\sim$ 450 cm^{-1}($v3$), the peak is attributed to the vibration of the B–O bond. In the range of 450 $\sim$ 700 cm^{-1}($v2$), the peak is linked with the oxygen octahedral vibration. Other Raman modes over 700 cm^{-1}($v1$) denote the overlapping bands of A1 (optical) and E (longitudinal optical) [34]. Moreover, as the BSS content increases, the peak value of $v2$ decreases, indicating that the average polarizability of B-site ions decreases. $v2$ mode shows the red shift characteristics because $NaNbO_3$ is replaced by heavier atoms. Simultaneously, an obvious broadening of the Raman peaks near 600 cm^{-1}($v2$) can be ascribed to the enhancement of the dielectric relaxation behavior and the growth of structural disorder [35].

The SEM images of the $(1 − x)$NN-xBSS ceramics are shown in Fig. 4, all samples were polished and thermal etching. The images show that the sample
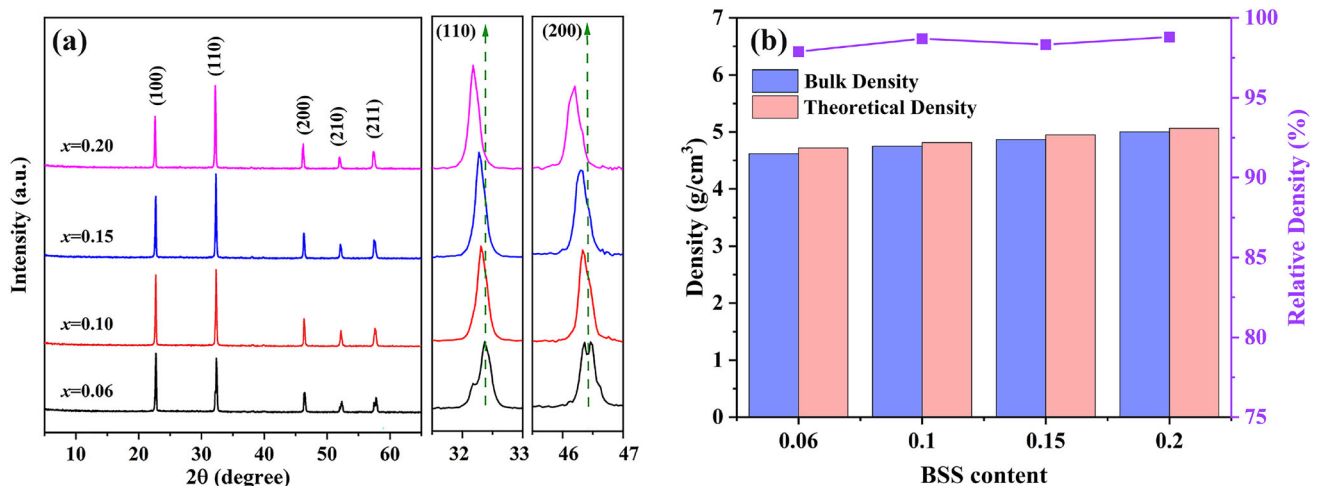

Fig. 1 a XRD patterns of the $(1 − x)$NN-xBSS ceramics. The magnified patterns of the (110) and (200) peak. **b** Bulk, theoretical and relative density of the $(1 − x)$NN-xBSS ceramics
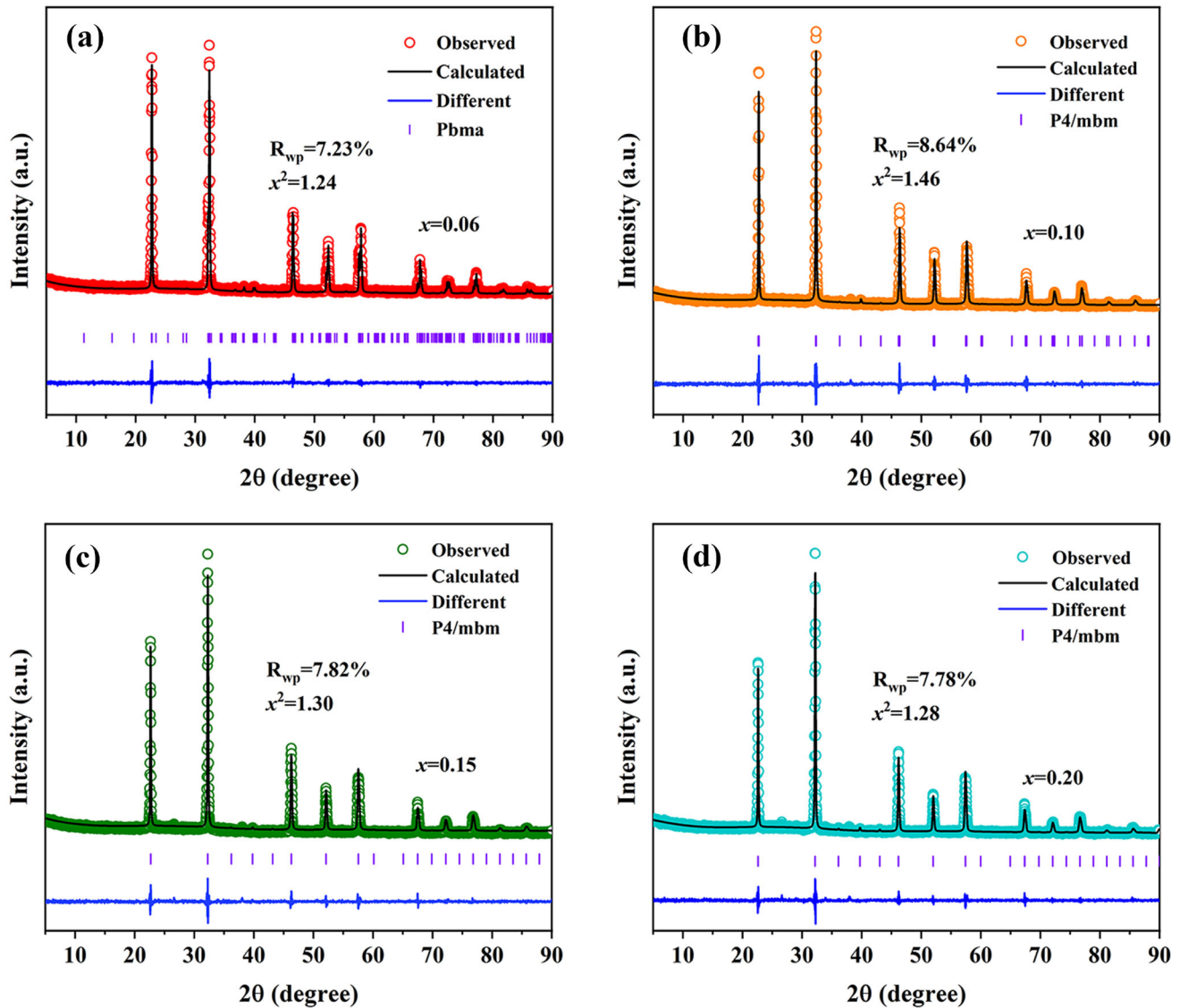
Fig. 2 The Rietveld refinement results of XRD patterns of $(1 - x)$ NN-xBSS ceramics. **a** $x = 0.06$, **b** $x = 0.10$, **c** $x = 0.15$, and **d** $x = 0.20$

particles are closely arranged and devoid of obvious pores when $x \geq 0.10$. As shown in Fig. 4a–d, the average particle sizes of the samples are 4.99 μm, 0.81 μm, 0.81, and 1.22 μm, respectively. With the increase of doping BSS, the average particle size decreases first and then increases. Additionally, the distribution of grain size is more uniform in $x = 0.10$ and 0.15 than in $x = 0.20$. The addition of Bi^{3+}, Sr^{2+}, and Sn^{4+} into $NaNbO_3$ will increase the lattice strain energy, which will be conducive to inhibiting the migration of grain boundaries and thus reducing the grain size [36]. With the increase of BSS content, the radius mismatch caused by doped ions or lattice expansion caused by Bi_2O_3 with low melting temperature leads to the abnormal grain growth [37].

3.2 Dielectric responses

Temperature dependence of permittivity (ε_r) and dielectric loss (tanδ) from − 150 to 300 °C with different frequencies for the $(1 - x)$NN-xBSS ceramics are plotted in Fig. 5 (a–d). In the same sample, the dielectric constant decreases as the frequency increases. At the same frequency, the maximum
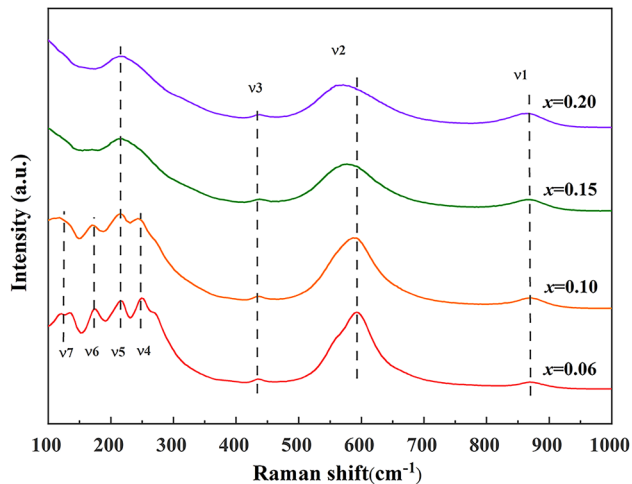
Fig. 3 Raman spectra of $(1-x)$ NN-xBSS ceramics at room temperature

value of the dielectric constant (ε_m) increases and then decreases with the increase of BSS doping. In addition, the small peak observed around 0 °C is believed to be caused by the transition from liquid water to solid ice (water peak) [38]. Specifically, a sharp dielectric peak was observed around 250 °C at

$x = 0.06$, which is associated with the transition from the AFE orthogonal P phase to the PE phase, indicating the presence of the AFE P phase at room temperature [39]. As the BSS content increases, the dielectric peak suddenly moves near -120 °C at $x = 0.10$, and the T_m decreases below room temperature indicating that the sample starts to transform into a paraelectric phase at room temperature, which is consistent with the results of XRD analysis. In Fig. 5 (b), a clear dispersion phase transition (at $x = 0.06$, the dielectric peak is sharper and at $x = 0.10$, the dielectric peak widens) and frequency dispersion (as the testing frequency increases, the dielectric constant decreases, and the temperature corresponding to the dielectric peak shifts toward high temperature) can be observed, proving the existence of relaxation properties. At $x = 0.15$ and 0.20, the dielectric peaks cannot be observed in the range of -150 to 300 °C, but it can be assumed that the dielectric peaks are below -150 °C based on the characteristics of Fig. 5c and d. According to the classification method of the researcher N. N. Krainik, NN-ABO$_3$ solid solutions can be divided into two
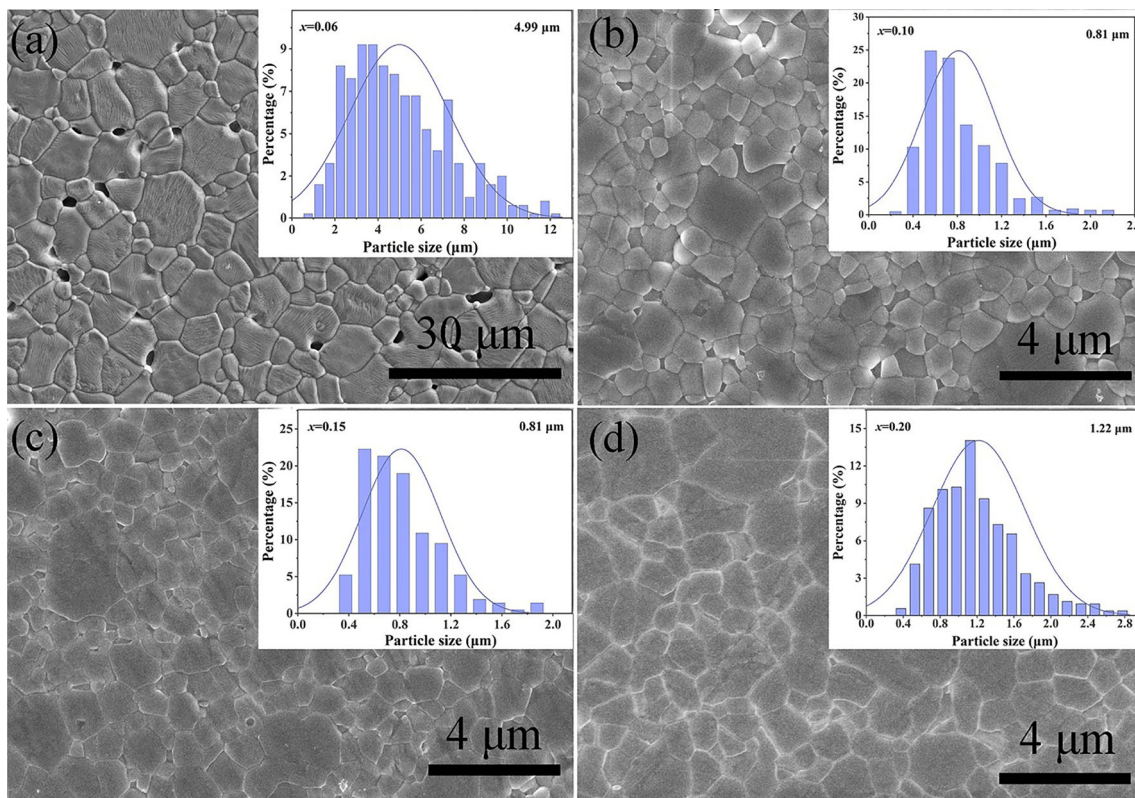

Fig. 4 SEM images of polished and thermally etched surfaces of $(1-x)$NN-xBSS ceramics with compositions of **a** $x = 0.06$, **b** $x = 0.10$, **c** $x = 0.15$, and **d** $x = 0.20$ and corresponding particle size distribution diagrams
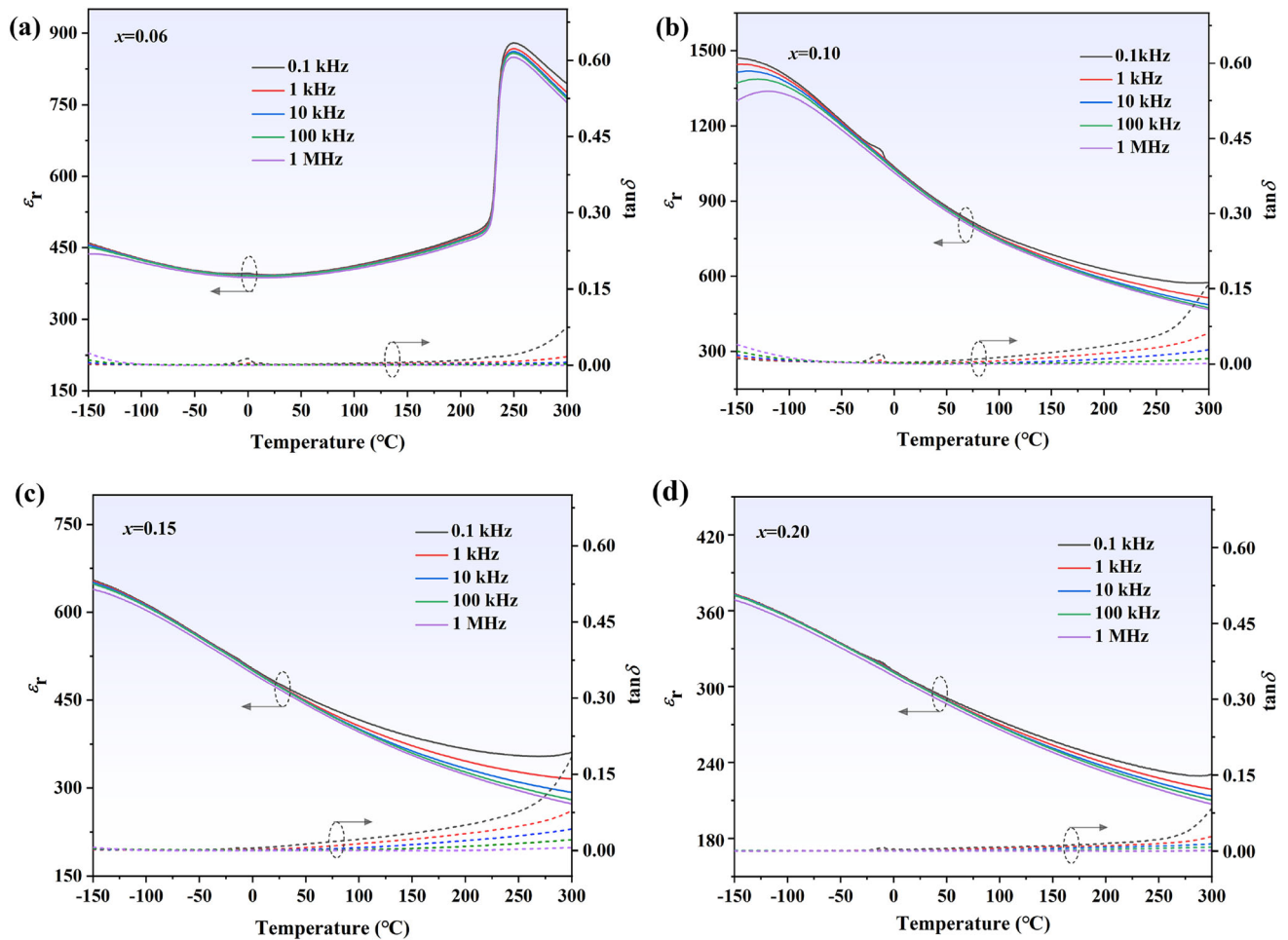
Fig. 5 Temperature dependence of dielectric permittivity and loss of $(1 - x)$NN-xBSS ceramics: **a** $x = 0.06$, **b** $x = 0.10$, **c** $x = 0.15$, and **d** $x = 0.20$

categories [40]. In the first category, the doping of a small amount of ABO_3 into the NN ceramics results in a sharp high-temperature dielectric peak, and in the second category, the T_m shifts sharply from the high-temperature to the low-temperature region when the doping of ABO_3 exceeds a certain critical value. From the above classification, it can be seen that $(1 - x)$NN-xBSS ceramics should belong to the second type, whose critical concentration should be between 0.06 and 0.10. After the doping of BSS exceeds the critical value, the T_m of the sample will drop abruptly from the high-temperature region to below room temperature. The dielectric loss of all samples is less than 0.075 in the temperature range of -150 to 200 °C, indicating that the stability of the samples is good in this temperature range.

For further assessment of the degree of relaxation behavior, the temperature dependence ε_r (at 10 kHz)

above T_m is matched by the modified Curie–Weiss law using following formula (5) [41, 42]:

$$\frac{1}{\epsilon_r} - \frac{1}{\epsilon_m} = \frac{(T - T_m)^{\gamma}}{C} \quad (T > Tm), \tag{5}$$

where parameters C and γ represent the Curie–Weiss-like coefficient and the value of the diffusion coefficient, respectively. In general, $\gamma = 1$ in the ordinary ferroelectric state and $\gamma = 2$ in the ideal relaxation ferroelectric state. As shown in Fig. 6a, the γ of the value increases from 1.64 to 1.71, demonstrating the enhancement of relaxation behavior in $x = 0.10$. In the $(1 - x)$ NN-xBSS system, due to the addition of cations (Bi^{3+}, Sr^{2+}, Sn^{4+}) that are not equivalent to Na^+ and Nb^{5+}, the substitution of ions at A and B sites will lead to local charge imbalance and structural distortion, thus destroying the long-range ordered ferroelectric domains of $NaNbO_3$ ceramics to form polar nano-regions (PNRs). These PNRs
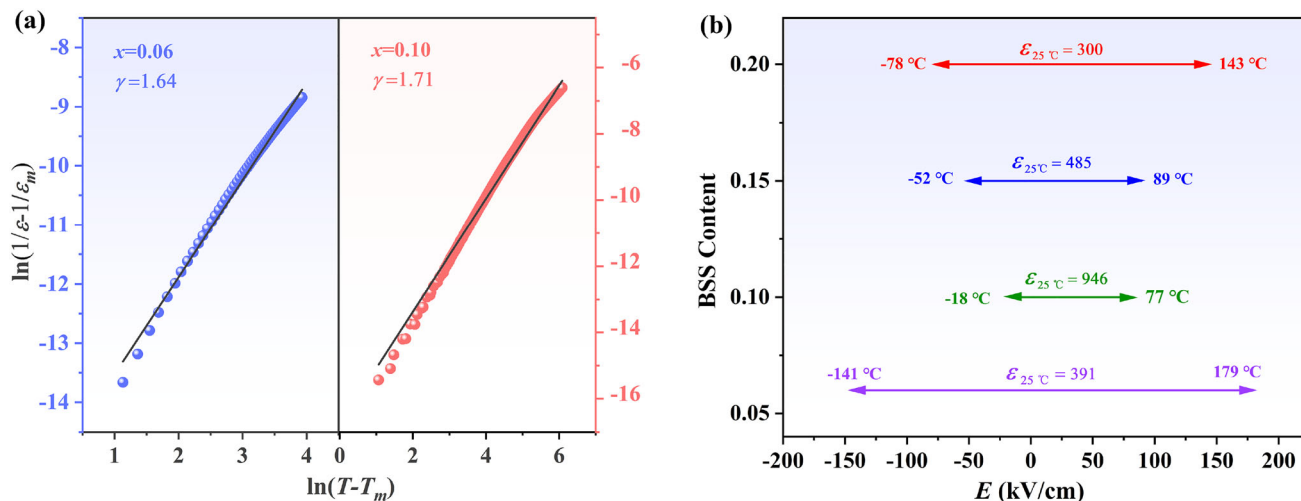
Fig. 6 **a** $\ln(1/\epsilon - 1/\epsilon_m)$ as a function of $\ln(T - T_m)$ at 10 kHz. **b** The temperature range of $\Delta\varepsilon/\varepsilon\,25°C$ less than $\pm 15\%$

embedded in disordered substrates will lead to relaxation behavior [43, 44]. In addition, all samples present low dielectric loss (tan$\delta < 20\%$). The thermal stability of permittivity is evaluated by the following formula (6), which meets $\Delta\varepsilon/\varepsilon_{25°C} \leq \pm 15\%$:

$$\frac{\Delta\varepsilon}{\varepsilon_{25°C}} = \frac{\varepsilon_r - \varepsilon_{25°C}}{\varepsilon_{25°C}}, \qquad (6)$$

where ϵ_r and $\varepsilon_{25°C}$ represent the permittivity at the target temperature and 25 °C, respectively. The temperature range of deviation less than $\pm 15\%$ is shown in Fig. 6b. When $x = 0.06$ and 0.20, the ceramics maintain a stable dielectric constant ($\Delta\varepsilon/\varepsilon_{25°C} \leq \pm 15\%$) in a wide temperature range (−141–179 °C, −78–143 °C), which shows that 0.94NN–0.06BSS and 0.80NN–0.20BSS ceramics meet the requirements of EIA X7R MLCC. When $x = 0.10$ and 0.15, −18–77 °C and − 52 to 89 °C satisfy $\Delta\varepsilon/\varepsilon_{25°C} \leq \pm 15\%$, respectively. Obviously, with the increase of BSS content, the thermal stability of permittivity first decreases and then increases, which is related to the position of the dielectric phase transition peak. Since the position of the dielectric phase transition peak is farther from the room temperature at $x = 0.06$ and 0.20, the dielectric constant stability has a wider temperature range.

Figure 7 presents the permittivity and dielectric loss of the $(1 - x)$ NN-xBSS ceramics as a function of the frequency at room temperature. The permittivity and dielectric loss of all samples are close to a parallel line, which proves that the samples have excellent frequency stability. Moreover, when the frequency is
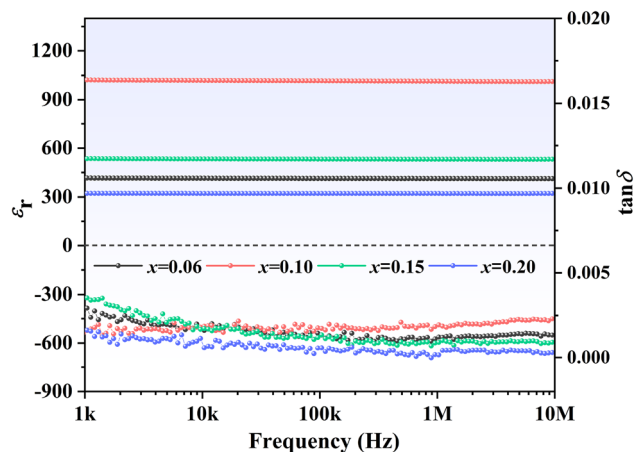

Fig. 7 Dielectric frequency spectra of $(1 - x)$ NN-xBSS ceramics

less than 100 kHz, there are slight fluctuations in the tanδ of each component, and when the frequency is greater than 100 kHz, the tanδ of each component is closer to a parallel line. As the amount of BSS doping increases, the tanδ first increases and then decreases. Overall, the tanδ values of all components are relatively close and remain at a very low value of less than 0.5%, which is crucial for device applications. The high dielectric loss may be related to defects in crystals, which restricts the enhancement of energy storage. The permittivity initially rises and subsequently falls with the increase of BSS content. Specifically, the permittivity at room temperature is only 410 in $x = 0.06$, which increases sharply to a maximum value of 1010 in $x = 0.10$, the permittivity then reduces to 530 in $x = 0.15$, and the small permittivity value of 320 is observed in $x = 0.20$.

Medium permittivity and ultra-low dielectric loss are beneficial to obtain higher energy storage density.

3.3 Ferroelectric properties and corresponding energy storage performance

The $P–E$ loops are measured at their E_b to assess the energy storage performance of $(1 − x)$NN-xBSS ceramics (Fig. 8a). It is well known that pure NN ceramics present a large polarization hysteresis, leading to low energy storage efficiency, which limits their applications. In this work, the addition of the nonequivalent cations (Bi^{3+}, Sr^{2+}, and Sn^{4+}) causes a mismatched strain and local charge imbalance, resulting in a local random field that can destroy the long-range ordered structure and give rise to a relaxation behavior. As a result, the $P–E$ loops of $(1$

$− x)$NN-xBSS ceramics become slimmer than those of pure NN ceramics [45]. The inset of Fig. 8a shows the $I\text{-}E$ loops for $(1 − x)$NN-xBSS ceramics, where the presence of small peaks can be observed near the breakdown electric field in all samples, associated with the transition from sub-stable ferroelectric domains to PNRs upon withdrawal of the electric field [46]. Another current peak associated with the AFE-FE phase transition is observed at $x = 0.06$ because the applied electric field strength of 180 kV/ cm is not sufficient to fully induce the phase transition of AFE-FE in 0.94NN–0.06BSS ceramic, demonstrating that doping with a small amount of BSS can stabilize the antiferroelectric phase. Similar phenomena have also been observed in other low-doped NN ceramic systems [11]. The current peak observed at $x = 0.10$ is associated with the coexistence of PNRs and ferroelectric domains, indicating a gradual
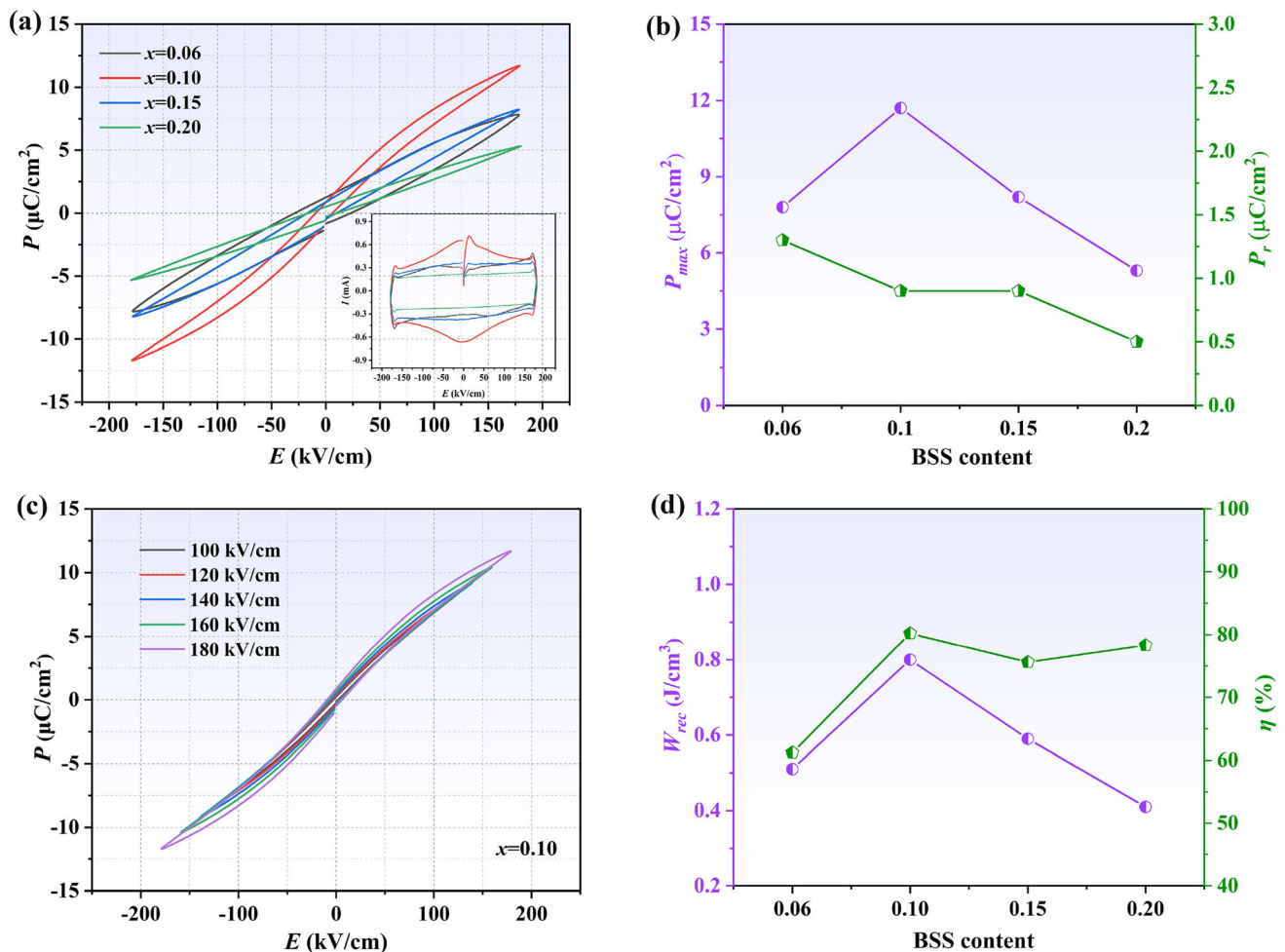

Fig. 8 a $P–E$ loops of $(1 − x)$NN-xBSS ceramics at their E_b. **b, d** The corresponding P_{max}, P_r, W_{rec}, and η as a function of BSS content. **c** $P–E$ loops of 0.90NN–0.10BSS ceramic under different electric fields

alignment of PNRs into long-ordered ferroelectric domains. As BSS doping further increases, the current peak becomes flat and gradually disappears. This result implies that the increase in BSS doping leads to the stable presence of PNRs. Figure 8b gives the P_{max} and P_r at their maximum electric field, respectively. In detail, the P_{max} value increases from 7.8 μC/cm^2 to 11.7 μC/cm^2, then decreases to 5.3 μC/cm^2, as well as the P_r value gradually reduces from 1.3 μC/cm^2 to 0.5 μC/cm^2 with increasing BSS content. Figure 8c exhibits the P–E loops in different electric fields when $x = 0.10$. Slim P–E loops are observed from 100 kV/cm to 180 kV/cm. In addition, the electric field dependence W_{rec} and η are calculated from the P–E loops (Fig. 8d). The best performance of the $(1-x)$NN-xBSS system is obtained when $x = 0.10$ (W_{rec}=0.80 J/cm^3, $\eta = 80.2\%$). Compared to 0.94NN–0.06BSS, W_{rec} increased by 57% and η increased by 31% for 0.90NN–0.10BSS, indicating that doping with BSS is beneficial in improving the energy storage properties of NN ceramics.

The frequency and temperature stability of energy storage efficiency are critical factors of dielectric capacitor materials that must be taken into account in practical applications. To evaluate the frequency stability of 0.90NN-0.10BSS ceramic, frequency dependence P–E loops as displayed in Fig. 9a is measured at 100 kV/cm with the frequency range of 1 to 50 Hz. The P–E loop expands when the frequency is 1 Hz, which is attributed to the slow changing rate of the electric field and the leakage current generated by the weak conductivity in ceramics. Furthermore, the corresponding change of

the W_{rec} and η is shown in Fig. 9b, the W_{rec} slightly changes from 0.30 J/cm^3 to 0.31 J/cm^3, and the η is between 84.3% and 93.1% with an acceptable variation of ∼ 9%. To evaluate the temperature stability of 0.90NN-0.10BSS ceramic, the P–E loops and the corresponding energy storage characteristics of 0.90NN-0.10BSS ceramic at different temperatures with an applied electric field of 100 kV/cm and a frequency of 10 Hz are shown in Fig. 10. There is a slight variation in the P–E loops from 20 to 60 °C and the P–E loop expands at 80 °C due to the increase in the conductivity of the sample as the temperature rises. As shown in Fig. 10 (b), as the temperature increases, W_{rec} decreases from 0.33 J/cm^3 to 0.27 J/cm^3 and η changes from 89.3 to 82.7% at 20–60 °C. When the temperature is 80, η reduces to 73.6% due to the increase in conductivity. Overall, the change in η is within the acceptable range (∼ 15%). Therefore, 0.90NN-0.10BSS ceramics exhibit frequency and temperature insensitivity within the testing range.

3.4 Charge–discharge performance

The charge–discharge performance for the 0.90NN-0.10BSS ceramic is measured to evaluate the power density and practical working performance. Figure 11a presents the effect of electric field on under-damped discharge characteristics of the 0.90NN–0.10BSS ceramic. The current peak (I_{max}), current density ($C_D=I_{max}/S$), and power density ($P_D=EI_{max}/2S$) increase with the raising electric field as shown in Fig. 11b. As the electric field increases from 40 to 100 kV/cm, I_{max} increases from 28.0 to 84.2 A, C_D
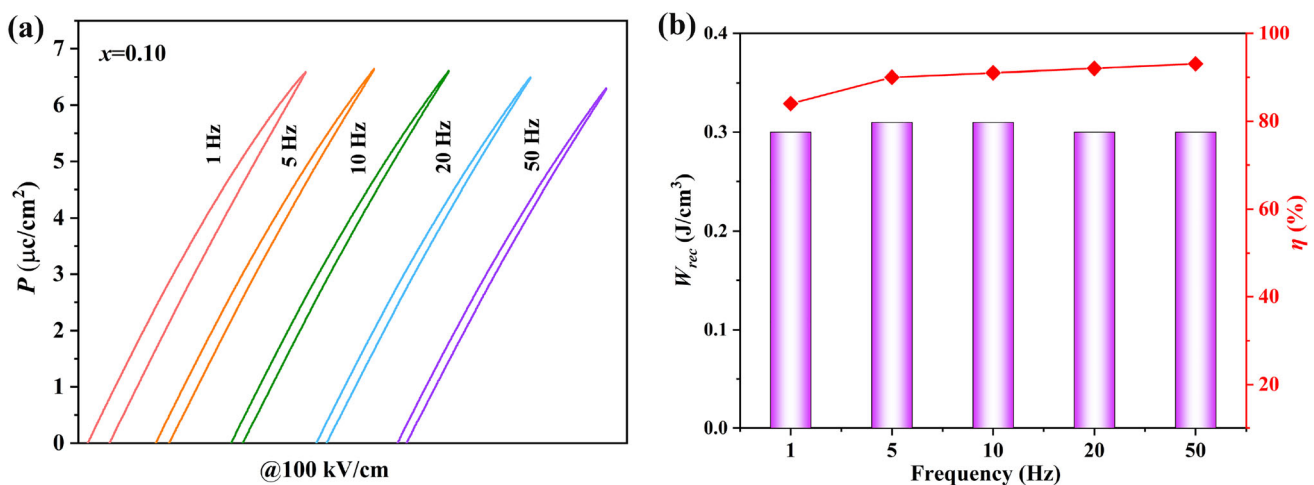

Fig. 9 Frequency characteristics of 0.90NN-0.10BSS ceramic **a** P–E loops and **b** the corresponding W_{rec} and η at different frequencies
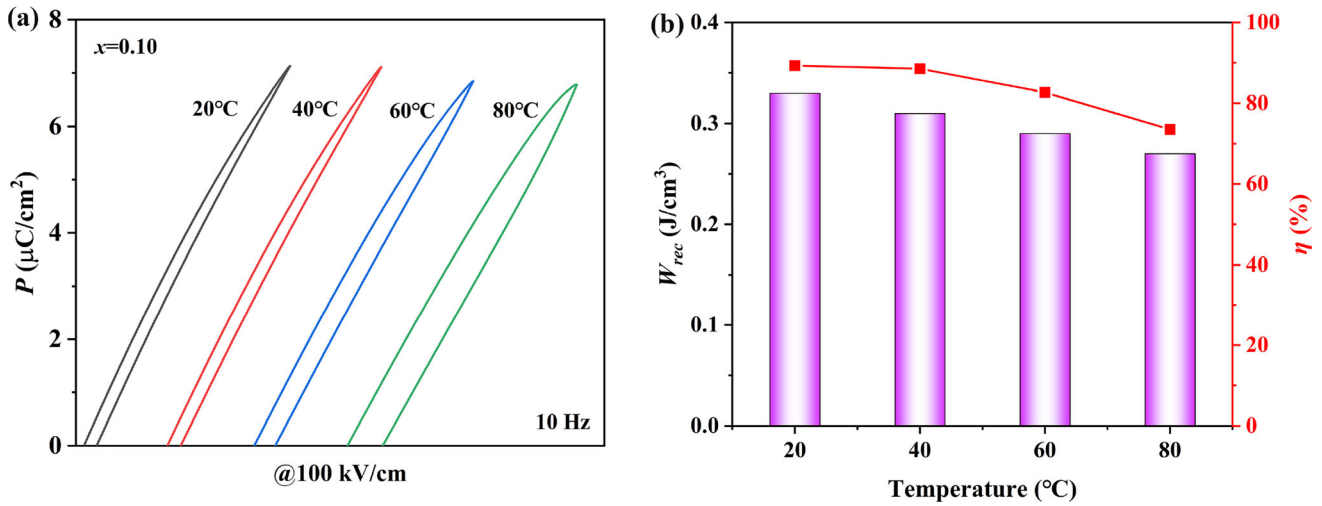
Fig. 10 Temperature characteristics of 0.90NN-0.10BSS ceramic **a** P–E loops and **b** the corresponding W_{rec} and η at different temperatures
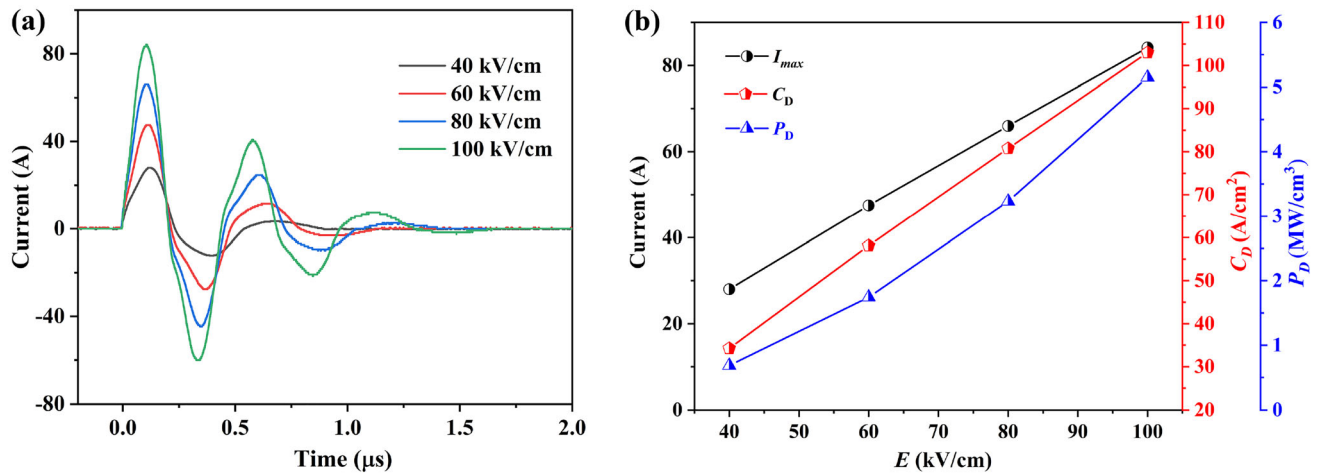

Fig. 11 a Effect of electric field on underdamped discharge characteristics of the 0.90NN–0.10BSS ceramic at room temperature. **b** Variations of I_{max}, C_D, and P_D as functions of the applied electric field

increases from 34.3 to 103.0 A/cm², and P_D increases from 0.69 to 5.2 MW/cm³. Obviously, I_{max}, C_D, and P_D have an approximately positive proportional relationship with electric field, which indicates that 0.90NN-0.10BSS ceramic has stable discharge characteristics. Overdamped discharge curves as a function of the electric field (40–100 kV/cm) are displayed in Fig. 11a. The current reaches the peak value rapidly and the duration of discharge is less than 2 µs. The discharge energy density (W_d) could be calculated according to formula (7):

$$W_d = \frac{R \int i(t)^2 dt}{V}, \tag{7}$$

where V is the sample volume and R is the load resistor (250.5 Ω). The inset of Fig. 12a presents the variation of W_d, I_{max}, and the corresponding time ($t_{0.9}$, the discharging time when 90% saturation value of W_d is released) with the electric field. The I_{max} increases from 2.5 to 6.5 A and W_d raises from 0.033 J/cm³ to 0.189 J/cm³ when electric field is from 40 to 100 kV/cm. In addition, $t_{0.9}$ as shown in Fig. 12b is used to evaluate the W_d−T curve of discharge rate and remains at ∼ 1 µs in the range of the tested electric field, indicating the discharge rate stability of 0.90NN-0.10BSS ceramic under different electric fields. The stability of the discharge time
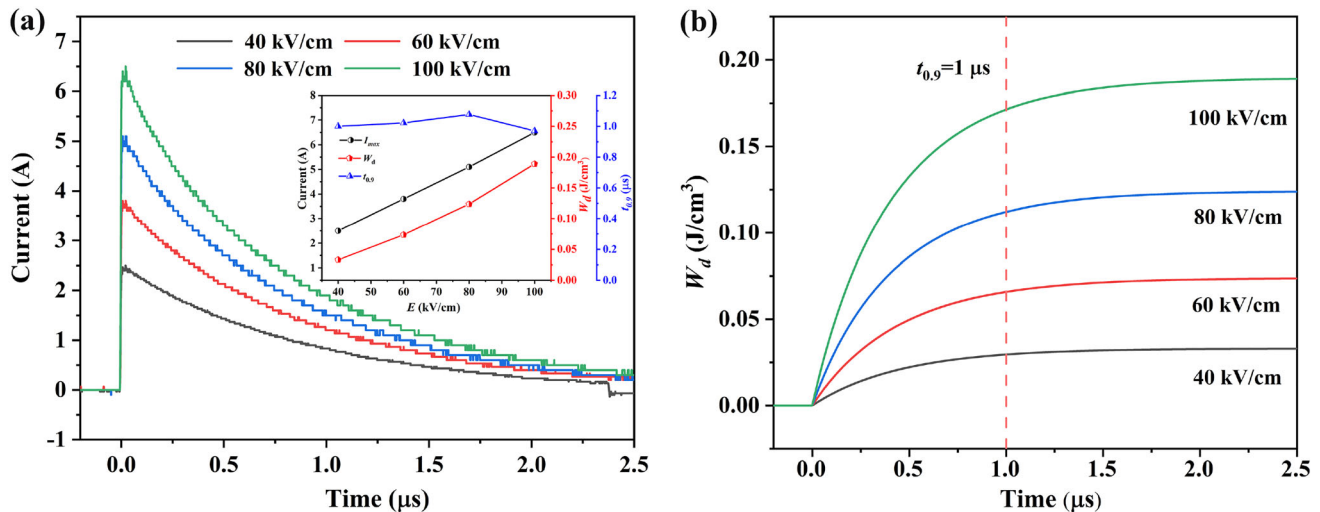
Fig. 12 Effect of electric field on overdamped discharge characteristics of 0.90NN-0.10BSS ceramic

under different electric fields is a desirable benefit for usage in a pulsed power system.

4   Conclusion

In conclusion, solid-state sintering successfully produced the $(1 - x)$NN-xBSS solid solutions with a pure perovskite structure. Firstly, the effect of doping with BSS on the phase structure was investigated by XRD and Raman spectroscopy, showing that doping with BSS converted the solid solution from an antiferroelectric phase (Pbma) to a paraelectric phase (P4/mbm). Secondly, as expected, the doping of BSS can stabilize the antiferroelectric phase. Furthermore, it was found that the doping of BSS disrupted the long-range ordering of the NaNbO$_3$ ceramics and formed PNRs, leading to a relaxation behavior that favors an increase in energy storage efficiency. The best performance of the $(1 - x)$NN-xBSS system was obtained when $x = 0.10$ (W_{rec} = 0.80 J/cm^3, η = 80.2%). The W_{rec} of 0.90NN-0.10BSS ceramic increased by 57% compared to 0.94NN-0.06BSS ceramic, as well as the η of 0.90NN-0.10BSS ceramic increased by 31%, indicating that the doping of BSS is beneficial in improving the energy storage performance of NN ceramics.

Acknowledgements

Author contributions

All authors contributed to the study conception and design. Material preparation, data collection, and analysis were performed by Yuqing Chen and Xinrong Zhong. The first draft of the manuscript was written by Yuqing Chen and all authors commented on previous versions of the manuscript. All authors read and approved the final manuscript.

Data availability

The data used to support the findings of this study are included within the article.

Declarations

Conflict of interest   The authors declare that they have no known competing financial interests or personal relationships that could have appeared to influence the work reported in this paper.

Ethical approval   The authors formally declare that the present paper is complied with ethical standards.

References

1. K. Zou, Y. Dan, H. Xu, Q. Zhang, Y. Lu, H. Huang, Y. He, Mater. Res. Bull. **113**, 190–201 (2019). https://doi.org/10.1016/j.materresbull.2019.02.002
2. F. Li, J. Zhai, B. Shen, H. Zeng, J. Adv. Dielectr. **08**, 1830005 (2018). https://doi.org/10.1142/S2010135X18300050

3. D. Hou, H. Fan, A. Zhang, Y. Chen, F. Yang, Y. Jia, H. Wang, Q. Quan, W. Wang, Ceram. Int. **47**, 34059–34067 (2021). https://doi.org/10.1016/j.ceramint.2021.08.315

4. P. Zhao, Z. Cai, L. Chen, L. Wu, Y. Huan, L. Guo, L. Li, H. Wang, X. Wang, Energ. Environ. Sci. **13**, 4882–4890 (2020). https://doi.org/10.1039/D0EE03094E

5. H. Qi, A. Xie, A. Tian, R. Zuo, Adv. Energy Mater. **10**, 1903338 (2020). https://doi.org/10.1002/aenm.201903338

6. K. Han, N. Luo, S. Mao, F. Zhuo, L. Liu, B. Peng, X. Chen, C. Hu, H. Zhou, Y. Wei, J. Mater. Chem. A **7**, 26293–26301 (2019). https://doi.org/10.1039/C9TA06457E

7. X. Hao, J. Adv. Dielectr. (2013). https://doi.org/10.1142/S2010135X13300016

8. Z. Dai, J. Xie, W. Liu, X. Wang, L. Zhang, Z. Zhou, J. Li, X. Ren, ACS Appl. Mater. Interfaces **12**, 30289–30296 (2020). https://doi.org/10.1021/acsami.0c02832

9. N. Luo, K. Han, M.J. Cabral, X. Liao, S. Zhang, C. Liao, G. Zhang, X. Chen, Q. Feng, J.-F. Li, Y. Wei, Nat. Commun. **11**, 4824 (2020). https://doi.org/10.1038/s41467-020-18665-5

10. Q. Yuan, G. Li, F.-Z. Yao, S.-D. Cheng, Y. Wang, R. Ma, S.-B. Mi, M. Gu, K. Wang, J.F. Li, H. Wang, Nano Energy. **52**, 203–210 (2018). https://doi.org/10.1016/j.nanoen.2018.07.055

11. H. Qi, R. Zuo, A. Xie, J. Fu, D. Zhang, J. Eur. Ceram. Soc. **39**, 3703–3709 (2019). https://doi.org/10.1016/j.jeurceramsoc.2019.05.043

12. J. Wang, H. Fan, M. Wang, P. Fan, Ceram. Int. **47**, 17964–17970 (2021). https://doi.org/10.1016/j.ceramint.2021.03.110

13. Y. Tian, L. Jin, H. Zhang, Z. Xu, X. Wei, G. Viola, I. Abrahams, H. Yan, J. Eur. Ceram. Soc. **5**, 17525–17531 (2017). https://doi.org/10.1039/C7TA03821F

14. L. Zhao, Q. Liu, S. Zhang, J.F. Li, J. Mater. Chem. C **4**, 8380–8384 (2016). https://doi.org/10.1039/C6TC03289C

15. Y. Tian, L. Jin, H. Zhang, Z. Xu, X. Wei, E.D. Politova, S.Y. Stefanovich, N.V. Tarakina, I. Abrahams, H. Yan, J. Mater. Chem. A **4**, 17279–17287 (2016). https://doi.org/10.1039/C6TA06353E

16. J. Gao, L. Zhao, Q. Liu, X. Wang, S. Zhang, J.F. Li, J. Am. Ceram. Soc. **101**, 5443–5450 (2018). https://doi.org/10.1111/jace.15780

17. H. Guo, H. Shimizu, C.A. Randall, Appl. Phys. Lett. **107**, 112904 (2015). https://doi.org/10.1063/1.4930067

18. D. Yang, J. Gao, L. Shu, Y.X. Liu, J. Yu, Y. Zhang, X. Wang, B.P. Zhang, J.F. Li, J. Mater. Chem. A **8**, 23724–23737 (2020). https://doi.org/10.1039/D0TA08345C

19. Y.I. Yuzyuk, P. Simon, E. Gagarina, L. Hennet, D. Thiaudière, V.I. Torgashev, S.I. Raevskaya, I.P. Raevskii, L.A. Reznitchenko, J.L. Sauvajol, J. Phys. : Condens. Matter. **17**, 4977 (2005). https://doi.org/10.1088/0953-8984/17/33/003

20. A. Xie, H. Qi, R. Zuo, ACS Appl. Mater. Interfaces **12**, 19467–19475 (2020). https://doi.org/10.1021/acsami.0c00831

21. S. Li, P. Shi, X. Zhu, B. Yang, X. Zhang, R. Kang, Q. Liu, Y. Gao, H. Sun, X. Lou, J. Mater. Sci. **56**, 11922–11931 (2021). https://doi.org/10.1007/s10853-021-06075-x

22. J. Shi, X. Chen, X. Li, J. Sun, C. Sun, F. Pang, H. Zhou, J. Mater. Chem. C **8**, 3784–3794 (2020). https://doi.org/10.1039/c9tc06711f

23. R.D. Shannon, C.T. Prewitt, Acta. Crystallorg. B **25**, 925–946 (1969). https://doi.org/10.1107/S0567740869003220

24. J. Ye, G. Wang, X. Chen, X. Dong, J. Materiomics. **7**, 339–346 (2021). https://doi.org/10.1016/j.jmat.2020.08.007

25. Z. Liu, J. Lu, Y. Mao, P. Ren, H. Fan, J. Eur. Ceram. Soc. **38**, 4939–4945 (2018). https://doi.org/10.1016/j.jeurceramsoc.2018.07.029

26. T. Pan, J. Zhang, Z.N. Guan, Y. Yan, J. Ma, X. Li, S. Guo, J. Wang, Y. Wang, Adv. Electron. Mater. **8**, 2200793 (2022). https://doi.org/10.1002/aelm.202200793

27. L. Zhao, Q. Liu, J. Gao, S. Zhang, J.F. Li, Adv. Mater. **29**, 1701824 (2017). https://doi.org/10.1002/adma.201701824

28. C. Liu, H. Yang, R. Hu, Y. Lin, J. Mater. Sci. Mater. Electron. **34**, 668 (2023). https://doi.org/10.1007/s10854-023-10009-5

29. Y. Pan, X. Wang, Q. Dong, J. Wang, H. Chen, X. Dong, L. Deng, H. Zhang, X. Chen, H. Zhou, Ceram. Int. **48**, 26466–26475 (2022). https://doi.org/10.1016/j.ceramint.2022.05.341

30. R.D. Shannon, Acta. Crystallorg. A **32**, 751–767 (1976). https://doi.org/10.1107/S0567739476001551

31. X. Dong, X. Li, X. Chen, H. Chen, C. Sun, J. Shi, F. Pang, H. Zhou, J. Materiomics. **7**, 629–639 (2021). https://doi.org/10.1016/j.jmat.2020.11.016

32. B. Toby et al., J. Appl. Crystallogr. **34**, 210–213 (2001). https://doi.org/10.1107/S0021889801002242

33. M. Zhou, R. Liang, Z. Zhou, X. Dong, J. Mater. Chem. A **6**, 17896–17904 (2018). https://doi.org/10.1039/C8TA07303A

34. A. Xie, J. Fu, R. Zuo, C. Zhou, Z. Qiao, T. Li, S. Zhang, Chem. Eng. J. (2022). https://doi.org/10.1016/j.cej.2021.132534

35. X. Zhao, Z. Zhou, R. Liang, F. Liu, X. Dong, Ceram. Int. **12**, 9060–9066 (2017). https://doi.org/10.1016/j.ceramint.2017.04.051

36. J. Ma, D. Zhang, F. Ying, X. Li, L. Li, S. Guo, Y. Huan, J. Zhang, J. Wang, S.T. Zhang, ACS Appl. Mater. Interfaces. **14**, 19704–19713 (2022). https://doi.org/10.1021/acsami.2c02086

37. Q. Hu, Y. Tian, Q. Zhu, J. Bian, L. Jin, H. Du, D.O. Alikin, V.Y. Shur, Y. Feng, Z. Xu, X. Wei, Nano Energy (2020). https://doi.org/10.1016/j.nanoen.2019.104264

38. P. Zhao, H. Wang, L. Wu, L. Chen, Z. Cai, L. Li, X. Wang, Adv. Energy Mater. (2019). https://doi.org/10.1002/aenm.201803048

39. J. Fu, R. Zuo, Acta Mater. **61**, 3687–3694 (2013). https://doi.org/10.1016/j.actamat.2013.02.055

40. I.P. Raevski, L.A. Reznitchenko, M.A. Malitskaya, L.A. Shilkina, S.O. Lisitsina, S.I. Raevskaya, E.M. Kuznetsova, Ferroelectrics. **299**, 95–101 (2004). https://doi.org/10.1080/00150190490429231

41. L.E. Cross, Relaxor ferroelectrics. Ferroelectrics. **76**, 241–267 (1987). https://doi.org/10.1080/00150198708016970

42. K. Uchino, S. Nomura, Ferroelectrics. **44**, 55–61 (1982). https://doi.org/10.1080/00150198208260644

43. X. Dong, X. Li, H. Chen, Q. Dong, J. Wang, X. Wang, Y. Pan, X. Chen, H. Zhou, J. Adv. Ceram. **11**, 729–741 (2022). https://doi.org/10.1007/s40145-022-0566-6

44. Q. Dong, X. Wang, J. Wang, Y. Pan, X. Dong, H. Chen, X. Chen, H. Zhou, Ceram. Int. **48**, 776–783 (2022). https://doi.org/10.1016/j.ceramint.2021.09.158

45. H. Shimizu, H. Guo, S.E. Reyes-Lillo, Y. Mizuno, K.M. Rabe, C.A. Randall, Dalton. Trans. **44**, 10763–10772 (2015). https://doi.org/10.1039/C4DT03919J

46. Q. Li, M.Y. Li, C. Wang, M. Zhang, H. Fan, Ceram. Int. **45**, 19822–19828 (2019). https://doi.org/10.1016/j.ceramint.2019.06.237